

X-ray Properties of the Abell 644 Cluster of Galaxies

Franz Bauer and Craig L. Sarazin

Department of Astronomy, University of Virginia, P.O. Box 3818, Charlottesville, VA 22903-0818;
feb4q@virginia.edu, cls7i@virginia.edu

ABSTRACT

We use new *ASCA* observations and archival *ROSAT* Position Sensitive Proportional Counter (PSPC) data to determine the X-ray spectral properties of the intracluster gas in Abell 644. From the overall spectrum, we determine the average gas temperature to be $8.64^{+0.67}_{-0.56}$ keV, and an abundance of $0.32 \pm 0.04 Z_{\odot}$. The global *ASCA* and *ROSAT* spectra imply a cooling rate of $214^{+100}_{-91} M_{\odot} \text{ yr}^{-1}$. The PSPC X-ray surface brightness profile and the *ASCA* data suggest a somewhat higher cooling rate. We determine the gravitational mass and gas mass as a function of radius. The total gravitating mass within 1.2 Mpc is $6.2 \times 10^{14} M_{\odot}$, of which 20% is in the form of hot gas. There is a region of elevated temperature 1.5-5' to the west of the cluster center. The south-southwest region of the cluster also shows excess emission in the *ROSAT* PSPC X-ray image, aligned with the major axis of the optical cD galaxy in the center of the cluster. We argue that the cluster is undergoing or has recently undergone a minor merger. The combination of a fairly strong cooling flow and evidence for a merger make this cluster an interesting case to test the disruption of cooling flow in mergers.

Subject headings: cooling flows — dark matter — galaxies: clusters: general — galaxies: clusters: individual (Abell 644) — intergalactic medium — X-rays: galaxies

1. Introduction

Cooling flows occur in clusters of galaxies where the age of the cluster has exceeded the cooling time scale of intracluster gas. In the more luminous clusters, this cooling time is comparable to the Hubble time (and thus cluster ages). Thus we should expect to see these flows, provided they have remained in hydrostatic equilibrium since formation. This result has been validated by studies with *Einstein*, *Ginga*, and *ROSAT* which indicate that cooling flows are common and long-lived phenomenon among nearby clusters (Edge et al. 1992; Peres et al. 1998).

Abell 644 (A644), with a bolometric luminosity exceeding 10^{45} ergs s $^{-1}$ and lying at a redshift of $z = 0.0704$, is one of the brighter clusters in the local universe. However, A644 is only a richness class 0 cluster (Abell, Corwin, & Olowin 1989), and thus has a higher than average X-ray luminosity for its richness class (typically $L_X = 10^{42-44}$ ergs s $^{-1}$; Abramopoulos & Ku 1983; Briel & Henry 1993). This cluster has been previously observed in X-rays with the *Einstein*, *Ginga*, and *ROSAT* observatories. The *Einstein* observations of A644 implied a significant cooling flow, with an accretion rate of $326 M_\odot \text{ yr}^{-1}$ (Edge et al. 1992), and an average gas temperature of 7.2 keV (David et al. 1993). More recent analysis of the *ROSAT* PSPC and HRI data imply slightly lower values of $\sim 200 M_\odot \text{ yr}^{-1}$ and 6.6 keV (Peres et al. 1998; White, Jones, & Forman 1997).

We present new *ASCA* X-ray spectra observations of A644 (§ 2). The use of *ASCA* spectra to determine the spatial variation of the spectral properties of the X-ray emitting gas in A644 requires that the effects of the energy-dependent point-spread function (PSF) be corrected. We also analyze archival *ROSAT* PSPC observations of the X-ray image and spectrum of A644. These spectra allow us to constrain global parameters (§ 3) as well as temperature variations and abundance gradients in the intracluster gas (§ 4). We use the *ASCA* derived temperature gradients and *ROSAT* derived X-ray surface brightness to determine the radial variation of the total gravitational mass and gas mass in the cluster (§ 6). We test the hydrostatic assumption by searching for evidence of asymmetries in the temperature distribution (§ 5), which would indicate recent dynamical activity, such as a subcluster merger. We also estimate the cooling rate (§ 7). We summarize our results and discuss their implications in § 8. Throughout this paper, we assume a Hubble constant $H_o = 50 \text{ km s}^{-1} \text{ Mpc}^{-1}$ and a cosmological deceleration parameter of $q_o = 0.5$. At a redshift of $z = 0.0704$, the angular diameter distance to the cluster is 375 Mpc, and $1'$ corresponds to 109 kpc. Unless otherwise stated, all errors are 90% confidence intervals for one parameter of interest.

2. Observations and Data Selection

A644 was observed with *ASCA* on 1995 April 18-20 for a total of 66.3 ksec with the two Gas Imaging Spectrometer (GIS) detectors and 58.3 ksec with the two Solid-State Imaging Spectrometer (SIS) detectors. The SIS observations were taken in 1 CCD faint mode, with the cluster center placed near the center of chip 1 of SIS0 and chip 3 of SIS1. We applied standard

cleaning procedures (Day et al. 1995), and selected data with a minimum cut off rigidity, elevation angle, and angle from the sunlit Earth of 6 GeV/c, 10° , and 25° , respectively. The screened exposure times were 49.5 ksec for the SIS detectors and 57.6 ksec for the GIS detectors.

We also retrieved the *ROSAT* PSPC observation of A644 from the archive (RP800379N00; PI: Böhringer). A644 was observed for 10.2 ksec on 1993 April 28-29. The PSPC data were filtered for periods of high background and other problems, and corrected for non-X-ray background, vignetting, and exposure using the computer programs developed by Snowden (Plucinsky et al. 1993; Snowden 1995). After filtering, the live exposure was 8.3 ksec. The average Master Veto Rate for the filtered data was 83.7.

The analysis of the global cluster spectrum and the *ROSAT* PSPC spectrum were done primarily with the XSPEC package (version 10.0), and the analysis of the PSPC image was done using the PROS package within IRAF. The deconvolution of the spatial variation of the spectrum from the energy-dependent Point Spread Function (PSF) of *ASCA* was performed using the algorithms of Markevitch (Markevitch 1996; Markevitch et al. 1998).

3. Global X-Ray Properties

Figure 1 shows a contour plot of the *ROSAT* PSPC X-ray image, superposed on a optical image from the Digital Sky Survey (Lasker et al. 1990). The image was corrected for background, vignetting, and exposure, and was smoothed with an adaptive kernel which gave a minimum signal to noise ratio of 5 per smoothing beam (Huang & Sarazin 1996). The cluster is fairly regular, but shows an asymmetric extension to the SSW in both the X-ray and the optical images; a similar extension was seen in the *Einstein* image (Mohr, et al. 1995). The cluster emission is strongly peaked on the position of the cD galaxy and the elongated X-ray structure is aligned with the cD major axis, an effect often seen in richer clusters.

The global X-ray spectrum of the cluster was determined by accumulating the spectra from the *ROSAT* PSPC and the *ASCA* GIS instruments in a circular region with a radius of $10'$. Beyond this radius, the X-ray surface brightness rapidly diminishes. We excluded the SIS instruments because the field of view (FOV) is only $11'$ square in 1 CCD mode, and doesn't cover the entire region used for the global cluster spectrum. However, including the SIS instruments does not significantly change the global results. The background for the *ASCA* observation was obtained from long exposure background fields at similar galactic latitude, and was extracted and cleaned identically to the data. The energy ranges adopted for the GIS was 0.6-10.0 keV. The background for the *ROSAT* PSPC spectrum was extracted from the same observation, using an annulus of $34-44'$ and masking out any point sources. The X-ray background was corrected for vignetting. Only energies from 0.24–2.5 keV were used for the fit to PSPC data. All of the channels used in the spectral fitting had more than 20 counts, so that the χ^2 distribution should be applicable.

Initially we fit both the *ASCA* and *ROSAT* data to a single temperature Raymond-Smith

optically thin thermal emission model (Raymond & Smith 1977), with the photoelectric absorption component (Morrison & McCammon 1984) fixed at the Galactic neutral hydrogen column density, $N_H^{gal} = 8.45 \times 10^{20} \text{ cm}^{-2}$ (Stark et al. 1992). We will refer to this model as the Single Temperature Model. A MEKAL Mewe-Kaastra thin-thermal plasma model (Mewe, Gronenschild, & van den Oord 1985; Kaastra 1992) was fit as an alternative, yielding nearly identical results. At first, we determined the temperature and overall heavy element abundance by fitting the *ASCA* and *ROSAT* spectra separately. The relative abundance ratios of heavy elements were fixed at the solar values given by Anders & Grevesse (1989).

The result of the single temperature fit to the *ASCA* GIS detectors is shown in the first row of Table 1 in the columns labeled “Single Temperature Model.” This is an acceptable fit, and gives reasonably well-determined values for the temperature and heavy element abundance. The result of the single temperature fit to the *ROSAT* PSPC spectrum is shown in the second row of Table 1. This fit is poorly constrained by the data. In addition, it gives a value for the abundance which is inconsistent with the value given by *ASCA*, and much higher than values found for similar clusters. The third row of Table 1 gives the result of a joint *ASCA* and *ROSAT* PSPC fit and is strongly skewed towards the *ASCA* results because the *ASCA* fit was more strongly constrained than that of the *ROSAT* data. Given the nearly disjoint energy ranges of *ASCA* and *ROSAT*, the conflict in the two spectral fits and the poor fit to the *ROSAT* spectrum suggest that the Single Temperature Model lacks a soft X-ray emission or absorption component which is present in the cluster. We consider two possibilities; an excess soft X-ray absorption or a cooling flow emission component.

First, we allowed the soft X-ray absorption to vary. This improved the fit somewhat, particularly for the *ROSAT* spectrum. In Table 1, we show the results of including an excess absorber with a column density of ΔN_H and a covering factor of unity at the redshift of the cluster (Excess Absorption Model). The combined fit of the data give an overall temperature of 7.59 keV, an overall heavy element abundance of 0.30 relative to solar, and an intrinsic absorption column of $\Delta N_H < 1.26 \times 10^{20} \text{ cm}^2$. The χ^2 for the fit with excess absorption is improved by 2.4 for one extra fitting parameter, which is significant at the 85% level for the f-test. However, the excess column is only about 15% of the nominal Galactic column of $N_H^{gal} = 8.45 \times 10^{20} \text{ cm}^{-2}$ (Stark et al. 1992), and thus could easily result from interpolating the H I data column to the position of the cluster. Moreover, for Galactic lines-of-sight with columns $N_H^{gal} \gtrsim 5 \times 10^{20} \text{ cm}^{-2}$ such as A644, there is a significant molecular component which increases the X-ray absorbing columns above those of H I (e.g., Arabadjijs & Bregman 1999). Thus, it seems likely that the small excess absorption required to fit the X-ray spectrum is Galactic in origin. However, the fact that the best-fit PSPC temperature is still completely inconsistent with the *ASCA* temperature indicates that a soft emission component is still missing.

Second, we added a cooling flow spectrum to the model, assuming the gas cooled isobarically subject to its own radiation from the ambient temperature in the central region to a very low temperature. The cooling gas had the same abundances as the ambient gas. The results are listed

in the third column of Table 1 (Cooling Flow Model). The global fit to *ASCA* GIS is significantly better. The *ROSAT* temperature, while barely bounded, is now consistent with *ASCA* and the abundances match. The fit to the *ROSAT* PSPC spectra is almost unchanged, indicating that these spectra do not require a cooling flow component. We derive a cooling rate of $214_{-91}^{+100} M_{\odot} \text{ yr}^{-1}$. In the combined fit, the addition of the cooling flow (with one more fitting parameter) decreases χ^2 by 16.9, which is a significant decrease at the 99.9% confidence level for the f-test. Thus, there is evidence for a cooling flow, at roughly the same rate as previous estimates.

The flux and luminosity, as derived from *ASCA* in the energy range of 2.0-10 keV are $5.45 \times 10^{-11} \text{ ergs cm}^{-2} \text{ s}^{-1}$ and $1.24 \times 10^{45} \text{ ergs s}^{-1}$, respectively, for a circular region with a radius of $10'$ centered on A644. Previous measurements with *Einstein* MPC gave a cluster temperature of $7.2_{-1.2}^{+1.8} \text{ keV}$, a flux and luminosity of $4.13 \times 10^{-11} \text{ ergs cm}^{-2} \text{ s}^{-1}$, and $9.55 \times 10^{44} \text{ ergs s}^{-1}$ using the 2-10 keV energy band and a circular aperture of $45'$ (David et al. 1993). The previous temperature, flux and luminosity results compare quite well with our global values. The global fits show that *ASCA* constrains both the thermal plasma temperature and heavy metal abundance better than *ROSAT* because of *ASCA*'s larger energy range and superior spectral resolution. Likewise, *ROSAT* determines the absorbing column and cooling rates better than *ASCA*, because of its lower energy range.

4. Radial Variation of the X-Ray Spectrum

4.1. Deconvolved *ASCA* Spectra

We determined the radial variation of the X-ray spectrum by accumulating *ASCA* spectra in 3 concentric annular regions centered on the cD galaxy with radii of 0-1.5', 1.5-5', and 5-10'. In Figure 2, the annuli are shown superposed on a contour plot of the *ROSAT* PSPC image. All of the annuli lie within the GIS FOV, while only the inner two regions, 0 – 1.5' and 1.5-5', fall fully within the SIS FOV. Thus we exclude the SIS from analysis of the outer region which only partially overlaps with the SIS detector. The annuli were chosen such that each was larger than the *ASCA* XRT+GIS PSF. We use methods developed by Markevitch (1996) to deconvolve the emission spectrum of the gas from the energy dependent PSF of *ASCA*. Because of its higher spatial resolution, we use the *ROSAT* PSPC image (Figure 1) to constrain the relative emission measure distribution between the regions. However, because of the possible contributions of a cooling flow or excess absorption in the central region, we do not fix the relative emission measure of this region from the *ROSAT* image, but allow it to vary. Due to the poor calibration of the *ASCA* telescope at low energies, we restrict our analysis to energies in the range 1.5-10 keV, excluding the gold edge from 2.0-2.5 keV. In addition to statistical errors, we include estimates of the systematic uncertainties of the background (20%, 1 σ), the PSF model's core (5%) and wings (15%), and the effective area of *ASCA* (5%), as suggested by Markevitch (1996). We also include the effect of the uncertainty in the offset between the *ASCA* and *ROSAT* images. The spectra

from each annulus and instrument were binned to insure that there were at least 20 counts per energy bin.

As evidenced from Figure 2, there is a moderately bright point source in the *ROSAT* PSPC image roughly $11'$ east of Abell 644. To ensure that this source is not contaminating the cluster emission in the outer regions, given *ASCA*'s broad PSF, we made an energy redistribution matrix which included this source as a separate region. For the source to truly be a contaminate, it should make up a significant percentage of the flux received from other regions. Our analysis indicates that this source contributes less than 1% of the flux in any of the regions used to accumulate the cluster spectrum.

The results of fitting the annular spectra are listed Table 2. The values of χ^2 given in the first row of the Table are for the simultaneous fit to all of the annuli. The *ASCA* temperatures are also plotted as a function of radius in Figure 3. The minimum value for χ^2 for all of the deconvolution fits of *ASCA* spectra are unrealistically low because of the inclusion of systematic errors (Markevitch 1996), which we have estimated pessimistically.

For the Single Temperature Model, the temperature in the central region is lower than that in the middle annulus, leading to a non-monotonic radial temperature variation. This low central temperature could be due to the reduction of the mean temperature in the central region by a cooling flow. We also consider the possibility that there is excess absorption toward the cooling flow. The inclusion of excess absorption alone in the spectrum of the central $0-1.5'$ region improved the fits somewhat, but the excess column is consistent with zero at the 90% confidence level. The best-fit value for the excess absorption of $\Delta N_H = 1.32 \times 10^{20} \text{ cm}^{-2}$ is again consistent with interpolation errors of the galactic absorption value or from the additional molecular component of the absorbing column.

Given the previous evidence from the X-ray surface brightness and spectra for a cooling flow at the center of A644, we included a cooling flow in the spectrum of the central $0-1.5'$ region in addition to the extra, intrinsic absorption. As in § 3, the gas was assumed to cool isobarically subject to its own radiation from the ambient temperature in that region to a very low temperature and had the same abundances as the ambient gas. The results of the Cooling Flow Model fits are also listed in Table 2. The inclusion of the central cooling flow increased the ambient gas temperature in the central region, but had no significant effect on the temperatures in the outer two annuli. The values of χ^2 were not reduced significantly from those of the Excess Absorption Model. The cooling rate was poorly determined.

We used both fixed ($Z = 0.30Z_\odot$) and variable abundance models, and found that they are not statistically different. The results of the variable abundance model are given in Figure 4 and Table 2. The middle annulus has a lower abundance, but it is possible that this is an artifact produced by the energy-dependent PSF of *ASCA*. In any case, the abundance is constant within the errors, even with the lower abundance in the middle annulus.

4.2. ROSAT PSPC Annular Spectra

The *ROSAT* PSPC spectra were accumulated in the same annuli as were used for the *ASCA* spectra. The results of fits to these spectra are shown in Table 3. As noted in the discussion of the global spectrum (§ 3), the PSPC spectra can strongly constrain the absorption or the cooling rate, but are relatively insensitive to the ambient gas temperature or the iron abundance. The central temperatures in the Single Temperature Model or the model with Excess Absorption disagreed strongly with the *ASCA* central temperature. For the outer two annuli, the *ROSAT* and *ASCA* temperatures were in reasonable agreement. The iron abundances, on the other hand, were rather high and almost unconstrained.

Allowing for excess absorption didn’t bring the *ROSAT* and *ASCA* temperatures into agreement. The excess absorption did not increase toward the center of the cluster, as has been found in other cooling flow clusters. This suggests that this excess absorption simply indicates that the Galactic absorption toward this cluster is underestimated by the interpolation of the H I measurements.

Finally, we included a cooling flow component in the spectra of the two inner regions; the results appear in the rightmost columns of Table 3. This model improved the fit of innermost region as well as the intrinsic absorption model did, but did not significantly change the fit of the $1'.5 - 5'$ region. The temperatures, although very poorly constrained, are now consistent with the *ASCA* values. We derive a cooling rate of $146 (< 380) M_{\odot} \text{ yr}^{-1}$ within the inner $0' - 1'.5$ region and $93 (< 392) M_{\odot} \text{ yr}^{-1}$ for the $1'.5 - 5'$ region.

5. Azimuthal Variations in the X-ray Spectrum

In order to search for azimuthal variations in the X-ray spectrum of A644, we further divided the second and third annular regions into four and two sectors, respectively. The geometry of the sectors is shown in Figure 2. The spectra were simultaneously fit to Single Temperature models, with the abundances allowed to vary (fixing abundance at 0.30 yielded results which were not statistically different from the variable abundance fits). The results of the variable abundance model are shown in Table 4. The temperatures and abundances are also plotted in Figures 5 and 6, respectively. We also did fits with central excess absorption and a central cooling flow, but these did not affect the parameters in the outer sections.

Table 4 and Figure 5 show that the high temperature found in the second annulus in the previous analysis (Table 2 and Figure 3) is the result of a very hot region to the west of the cluster center. The temperatures are inconsistent with an isothermal distribution or azimuthally symmetric distribution at $> 99.9\%$ level. However the temperatures are roughly consistent with an isothermal distribution if we exclude regions 3 and 5. On the other hand, the abundances are poorly determined, and there is no significant evidence for any spatial variation.

There is no point source in the *ROSAT* PSPC or HRI images in the high temperature western region, so it is unlikely that this spectral component is due to a background AGN or some other sources. We also examined the *ASCA* GIS and SIS images of this region in the 7-10 keV band, and found no evidence of a point source. This test was done to check whether the high temperature might be due to a strongly absorbed or highly variable AGN, which might have been unobservable by *ROSAT*. The hard X-ray emission which gives the western region of the cluster its very high temperature appears to be extended in the hard band GIS images.

6. X-ray Surface Brightness Profile and Masses

The *ROSAT* PSPC counts were extracted in annular regions of increasing size ($1' - 5'$) such that each region had an adequate number of counts. Bright point sources were excluded from these regions and X-ray background was subtracted from an annular region where cluster emission was negligible ($\approx 34 - 44'$). We used the results of the Cooling Flow Model fits to the global PSPC (Table 1) spectrum to convert the surface brightness into a physical flux. We also corrected the surface brightness for the nominal Galactic absorbing column of $N_H^{gal} = 8.45 \times 10^{20} \text{ cm}^{-2}$ (Stark et al. 1992). The resulting X-ray surface brightness is shown in Figure 7.

The *ROSAT* PSPC X-ray surface brightness was de-projected to determine the X-ray emissivity as a function of radius on the assumption that the cluster was spherically symmetric (see below). The gas density ρ was determined from the X-ray emissivity and the *ASCA* temperature profile obtained from the annular regions for the Single Temperature model (Figure 3). Because the *ASCA* temperatures were only determined in three radial bins, we linearly interpolated the temperature to determine the values at all radii. The gas density was integrated over the interior volume to give the gas mass as a function of radius, $M_{gas}(r)$. The assumption of hydrostatic equilibrium allows the gravitational mass M_{tot} within a radius r to be determined from

$$M_{tot}(< r) = -\frac{rkT(r)}{\mu m_H G} \left[\frac{d \ln \rho(r)}{d \ln r} + \frac{d \ln T(r)}{d \ln r} \right], \quad (1)$$

where T is the gas temperature, and μ is the mean particle mass in terms of the mass of hydrogen, m_H .

Because of the enhanced X-ray surface brightness to the SSW (Figure 1) and the very high temperature in region 3 to the west (Figure 3), it seems unlikely that the cluster is well-relaxed, at least in this area. On the other hand, the northern side of the cluster appears more regular. Thus, we only use sectors 1, 4, 5, and 7 (see Figure 2) to determine the gas density in de-projection. We used this modified gas density to calculate the gas and gravitational masses.

Figure 8 shows the accumulated gravitational mass (filled squares) and gas mass (crosses) profiles. The statistical errors for these masses cannot be easily assigned since the errors in the emissivities at different radii are correlated by the de-projection. Thus errors were generated by a Monte Carlo technique (Arnaud 1988; Irwin & Sarazin 1995). We randomly selected X-ray count

values for each radial bin from a Poisson distribution with a mean value equal to the number of counts in the actual data. We also generated a simulated temperature profile from randomly selected temperature values for each radial bin from a Gaussian distribution with a mean value equal to the actual temperature derived in that radial bin. We use these two profiles to simulate electron density, gas mass and gravitational mass profiles. We ran this Monte Carlo simulation 1000 times, sorted the values, and chose the 50th and 950th values to define the 90% confidence region. Figure 8 shows that the gas mass (the lower profile) accounts for 15% of the gravitational mass (the upper profile) at a radius of 300 kpc, increasing to 20% at 1.2 Mpc.

7. Cooling Mass Deposition Rate

The cooling radius, r_c , is defined as the radius at which the integrated cooling time is equal to the age of the cluster, for which we assume an age of 10^{10} yr. For every radius for which the de-projection gave a value of the gas density, we calculated the integrated cooling time in the gas. The heavy element abundance is fixed at 30% of solar. From the derived density profile, we obtained a cooling radius $r_c = 261_{-64}^{+376}$ kpc

We determined the cooling rate profile using the technique outlined in Arnaud (1988), which assumes a steady-state cooling flow. Using the de-projected X-ray emissivity, we determine the X-ray luminosity output from each de-projected spherical shell. The luminosity from a given shell is assumed to result from the combination of gas cooling out of the flow in that shell, and gas flowing into that shell but not cooling below X-ray emitting temperatures. The rate at which mass drops out of the flow in shell i , $\Delta\dot{M}_i$, is taken to be

$$\Delta\dot{M}_i = \frac{\Delta L_i - \dot{M}_{i-1}(\Delta H_i + \Delta\phi_i)}{H_i + f_i\Delta\phi_i}, \quad (2)$$

where ΔL_i is the change in bolometric luminosity across shell i , \dot{M}_{i-1} is the rate at which mass passes through shell i but does not cool out of the flow, $H_i = 5kT(r)/2\mu m_H$ is the enthalpy per unit mass in shell i , ΔH_i is the change in H_i across that shell, $\Delta\phi_i$ is the change in potential across shell i , and f_i is a geometrical factor to allow for the fact that mass cools out of the flow in a volume-averaged way. We determine the gravitation potential assuming hydrostatic equilibrium as discussed in § 6. This gives

$$\phi(r) - \phi(0) = - \int_0^r \frac{kT(r)}{\mu m_H} [d \ln \rho(r) + d \ln T(r)] , \quad (3)$$

where $\phi(0)$ is the potential at the center of the cluster.

The total integrated cooling rate at a distance r is simply the sum of the mass dropping out of the flow in all the shells at radii less than r_n :

$$\dot{M}(< r_n) = \sum_{i=1}^n \Delta\dot{M}(r_i). \quad (4)$$

Figure 9 shows the resulting integrated cooling rate profile, along with the 5 and 95 percentile values from the 1000 Monte Carlo simulations. As noted above, this technique assumes a steady-state cooling flow, and thus may only apply out to $r_c = 261$ kpc. The total cooling rate out to this radius is $393 M_\odot \text{yr}^{-1}$. This is consistent but somewhat larger than the values derived spectroscopically.

8. Conclusions

The global X-ray spectrum of A644 is well fit by a model with a gas temperature of $7.69^{+0.22}_{-0.20}$ keV, and an abundance of $0.30 \pm 0.03 Z_\odot$. The global spectrum suggests that there is a cooling flow in the cluster with a cooling rate of $214^{+100}_{-91} M_\odot \text{yr}^{-1}$. The spectrum also suggests an absorbing column which is slightly larger than the interpolated Galactic H I column, but this may be due to small scale variations in the H I column or to molecular material. The excess absorption is not concentrated to the cluster center, so it is probably not intrinsic to the cooling flow or cluster.

We also determined the spatial variation of the temperature, iron abundance, and cooling rate. There is no significant evidence for any spatial variation in the iron abundance. We find evidence for a region of extremely hot gas (10-25 keV) located 1.5-5' to the west of the cluster center. This region is perpendicular to the enhanced emission in the *ROSAT* PSPC X-ray image. We suggest that the cluster is undergoing or has recently undergone a merger. The combination of a moderate cooling flow and evidence for a merger make this cluster an interesting case to test the disruption of cooling flows by mergers. Better spatial resolution data (e.g., with *Chandra* or *XMM*) is needed to confirm the merger in A644 and to determine its geometry.

We determined the X-ray surface brightness profile excluding the hot region to the west and the extended region to the SSW. We use the X-ray surface brightness and temperature profiles to determine the gas and gravitational masses as a function of radius. The total gravitating mass within 1.2 Mpc is $6.2 \times 10^{14} M_\odot$, of which 20% is in the form of hot gas. Since we have not included the mass from individual galaxies, this result gives a lower limit on the baryonic fraction within the cluster well above the upper limit from cosmic nucleosynthesis of 0.06 for an $\Omega = 1$ universe (e.g., Walker et al. 1991). The baryonic fraction of A644 is consistent with other clusters and groups (e.g., Allen & Fabian 1994; David et al. 1994).

This research has made use of data obtained through the High Energy Astrophysics Science Archive Research Center Online Service, provided by the NASA/Goddard Space Flight Center. F. E. B. and C. L. S. were supported in part by NASA ASCA grants NAG 5-4516 and NAG 5-8390. C. L. S. was also supported in part by NASA Astrophysical Theory Program grant NAG 5-3057. We would like to thank Maxim Markevitch for many helpful comments on the analysis of *ASCA* data. F. E. B. would like to thank Jimmy Irwin to his many helpful comments.

REFERENCES

- Abell, G. O., Corwin, H. G., & Olowin, R. P. 1989, *ApJS*, 70, 1
- Abramopoulos, F., & Ku, W. 1983, *ApJ*, 248, 429
- Allen, S. W., & Fabian, A. C. 1994, *MNRAS*, 269, 409
- Anders, E., & Grevesse, N. 1989, *Geochem. Cosmochim. Acta.*, 53, 197
- Arabadjis, J. S., & Bregman, J. N. 1999, *ApJ*, 510, 806
- Arnaud, K. A. 1988, in *Cooling Flows in Cluster & Galaxies*, ed. A. C. Fabian (Dordrecht: Kluwer), 31
- Briel, U. G., & Henry, J. P. 1993, *A&A*, 278, 379
- David, L. P., Slyz, A., Jones, C., Forman, W., Vrtillek, S. D., & Arnaud, K. A. 1993, *ApJ*, 412, 479
- David, L. P., Jones, C., Forman, W., & Daines, S. J. 1994, *ApJ*, 428, 544
- Day, C., Arnaud, K., Ebisawa, K., Gotthelf, E., Ingham, J., Mukai, K., & White, N. 1995, *The ABC guide to ASCA Data Reduction Version 4*, ASCA Guest Observer Facility, NASA Goddard Space Flight Center
- Edge, A. C., Stewart, G. C., & Fabian, A. C. 1992, *MNRAS*, 258, 177
- Huang, Z., & Sarazin, C. L. 1996, *ApJ*, 461, 622
- Irwin, J. A., & Sarazin, C. L. 1995, *ApJ*, 455, 497
- Kaastra, J. S. 1992, *An X-Ray Spectral Code for Optically Thin Plasmas* (Internal SRON-Leiden Report, updated version 2.0)
- Lasker, B. M., Sturch, C. R., McLean, B. J., Russell, J. L., Jenkner, H., & Shara, M. M. 1990, *AJ*, 99, 2019
- Markevitch, M. 1996, *ApJ*, 465, L1
- Markevitch, M., Forman, W. R., Sarazin, C. L., & Vikhlinin, A. 1998, *ApJ*, 503, 77
- Mewe, R., Gronenschild, E. H. B. M., & van den Oord, G. H. J. 1985, *A&AS*, 62, 197
- Mohr, J. J., Evrard, A., Fabricant, D. G., & Geller, M. J. 1995, *ApJ*, 447, 8
- Morrison, R., & McCammon, D. 1983, *ApJ*, 270, 709
- Peres, C. B., Fabian, A. C., Edge, A. C., Allen, S. W., Johnstone, R. M., & White D. A. 1998, *MNRAS*, 298, 416
- Plucinsky, P. P., Snowden, S. L., Briel, U. G., Hasinger, G., & Pfeffermann, E. 1993, *ApJ*, 418, 519
- Raymond, J. C., & Smith, B. W. 1977, *ApJS*, 35, 419
- Snowden, S. L. 1995, *Cookbook For Analysis Procedures for ROSAT XRT/PSPC Observations of Extended Objects and the Diffuse Background*

- Stark, A. A., Gammie, C. F., Wilson, R. W., Bally, J., Linke, R. A., Heiles, C., & Hurwitz, M. 1992, *ApJS*, 79, 77
- Walker, T. P., Steigman, G., Schramm, D. N., Olive, K. A., & Kang, H. 1991, *ApJ*, 376, 51
- White, D. A., Jones, C., & Forman, W. R. 1997, *MNRAS*, 292, 419

Fig. 1.— A contour plot of the *ROSAT* PSPC X-ray image in the 0.5–2.0 keV band after adaptive kernel smoothing. A minimum signal to noise ratio of 5 per smoothing beam was used. The contours are superposed on an optical image from the Digital Sky Survey (Lasker et al. 1990). The lowest contour level is 0.4 counts/pixel ($7''5$), with higher contours being spaced logarithmically (by a factor of $2^{1/2}$). Note the overall elliptical shape of the emission, which is elongated in the same direction as the central cD galaxy, and the region of enhanced X-ray emission about $5'$ to the south–southwest of the cluster center.

Fig. 2.— A contour plot of the the *ROSAT* PSPC X-ray image identical to (Figure 1) is shown. The dashed circle and square represent the FOV of the GIS2 and SIS0 instruments, respectively. Superposed are the annuli (0–1.5', 1.5–5', and 5–10') and sectors (1–7) used in the spectral fitting to determine the radial and azimuthal variation of the X-ray spectrum of A644.

Fig. 3.— The radial temperature profile in A644 determined from single temperature fits without excess absorption to *ASCA* spectra (solid squares, light lines) and *ROSAT* PSPC spectra (diagonal crosses, dark lines). The horizontal error bars give the widths of the annuli used. The values are plotted at the emission weighted mean radius derived from the *ROSAT* PSPC image. The vertical error bars represent the 90% confidence regions.

Fig. 4.— The radial profile of the heavy element (primarily iron) abundance in A644 from the *ASCA* spectra. The horizontal error bars give the widths of the annuli used. The values are plotted at the emission weighted mean radius derived from the *ROSAT* PSPC image. The vertical error bars represent the 90% confidence regions.

Fig. 5.— The temperatures determined from *ASCA* spectra for the sectors shown in Figure 2. Error bars represent the 90% confidence regions.

Fig. 6.— The abundances determined from *ASCA* spectra for the sectors shown in Figure 2. Error bars represent the 90% confidence regions.

Fig. 7.— The *ROSAT* PSPC X-ray surface brightness of A644 in radial annuli for the 0.5 – 2.02 keV band with error bars representing the 90% confidence regions.

Fig. 8.— The values of the interior gravitational mass (filled squares, upper points) and interior gas mass (no symbols, just error bars, lower points) derived from the *ROSAT* PSPC radial surface brightness profile and *ASCA* temperatures in annuli. Error bars represent the 90% confidence regions from 1000 Monte Carlo simulations.

Fig. 9.— The integrated cooling rate profile for the cluster. Error bars represent the 90% confidence regions from 1000 Monte Carlo simulations.

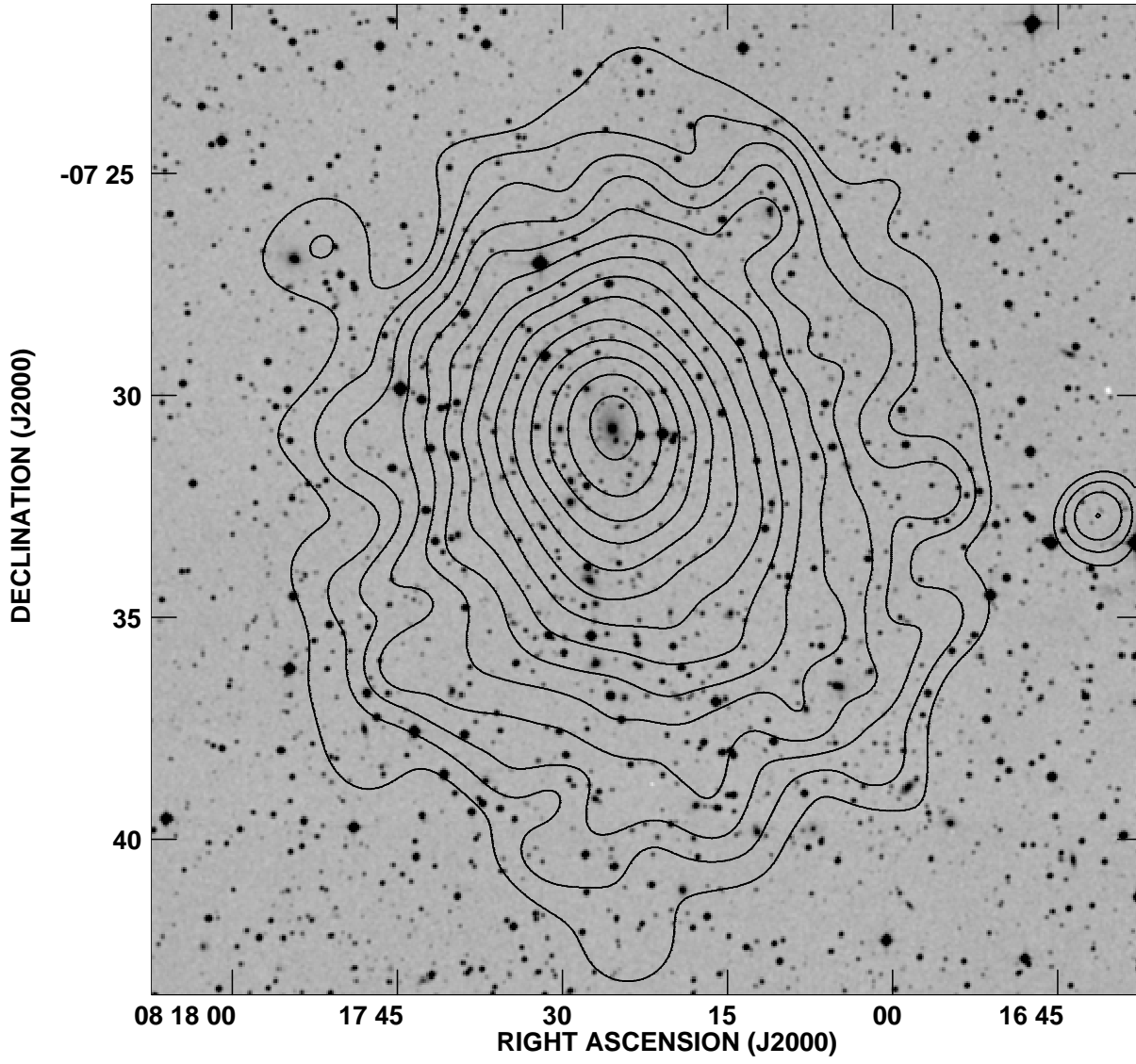


Figure 1

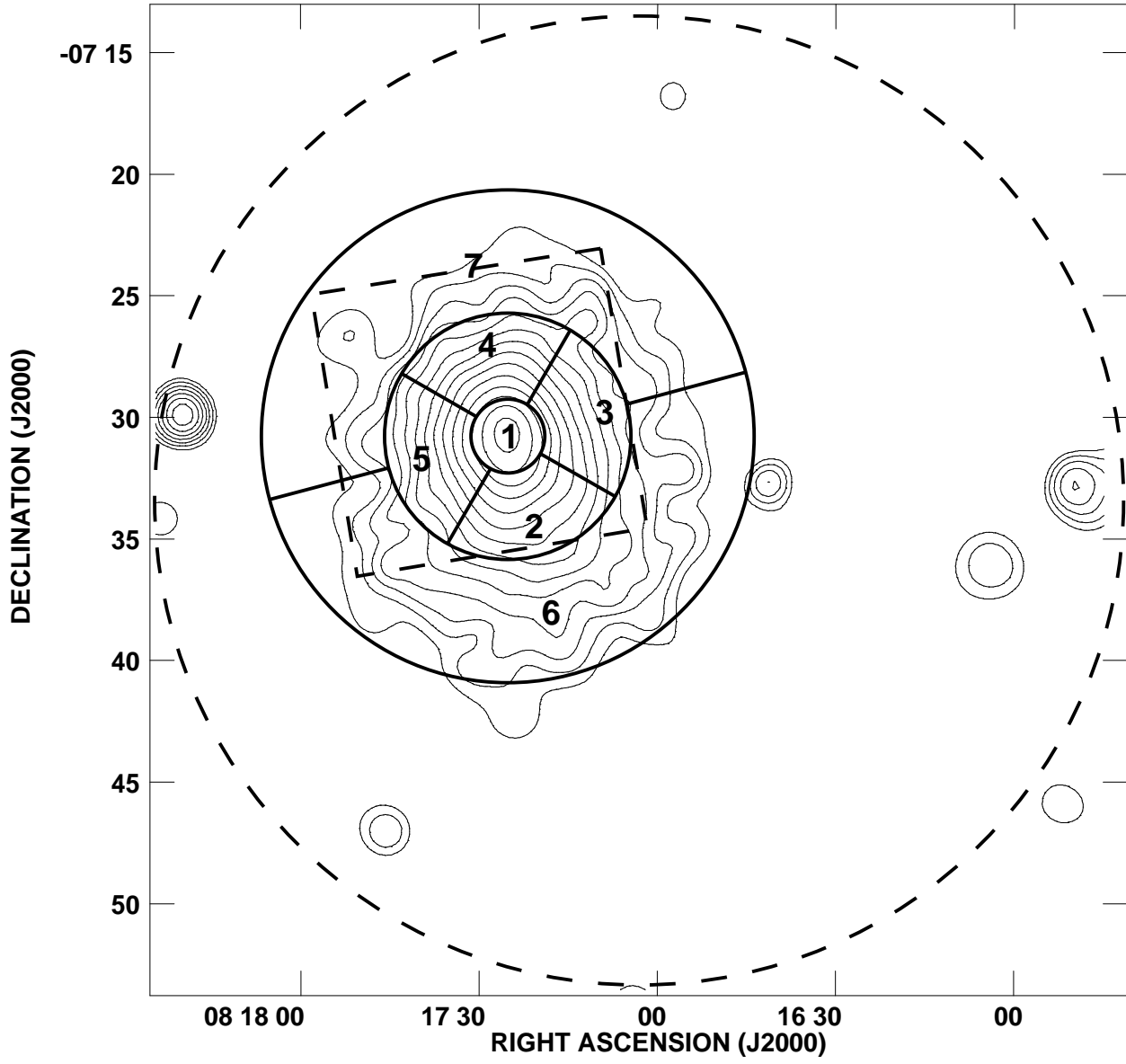


Figure 2

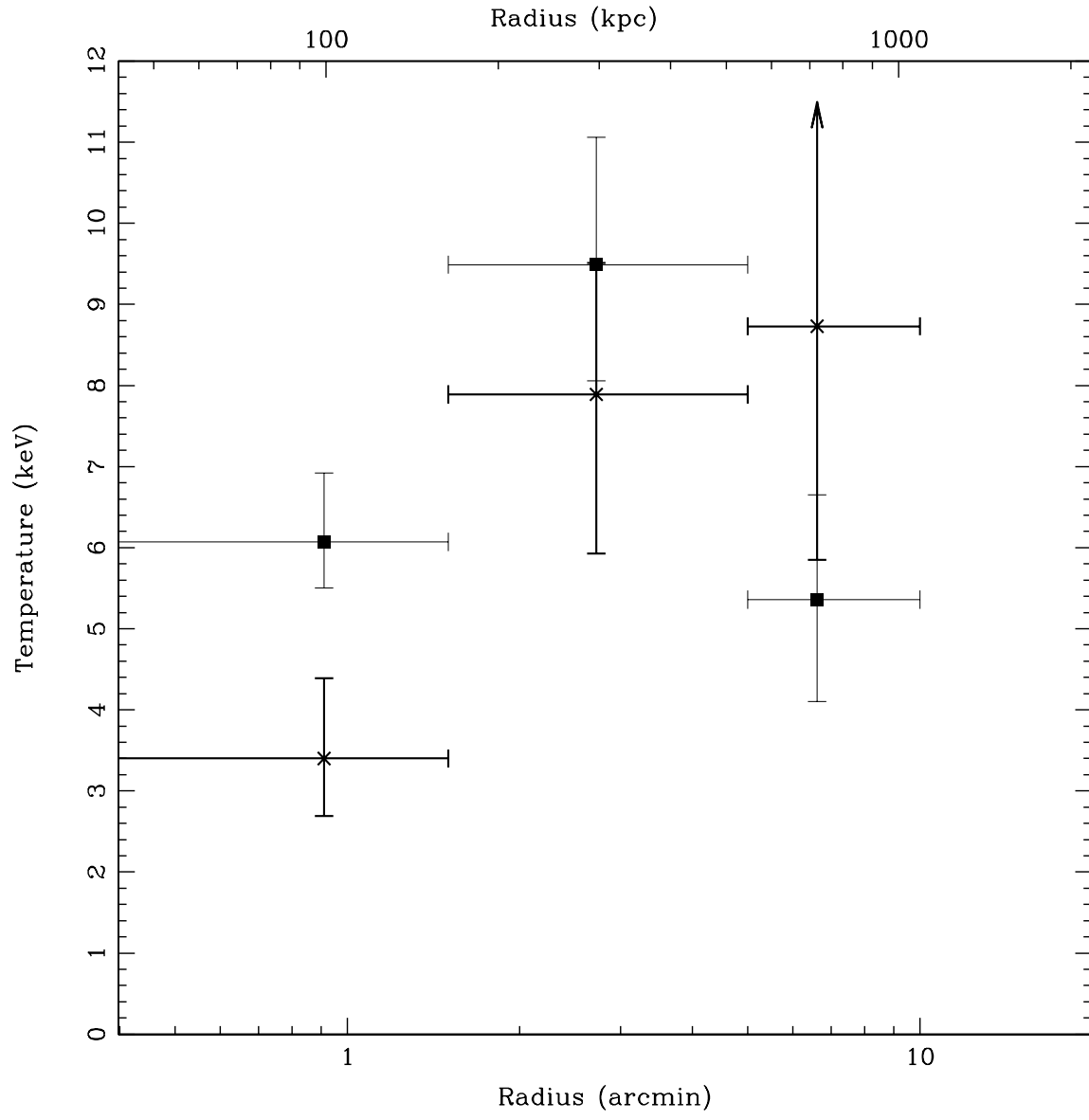


Figure 3

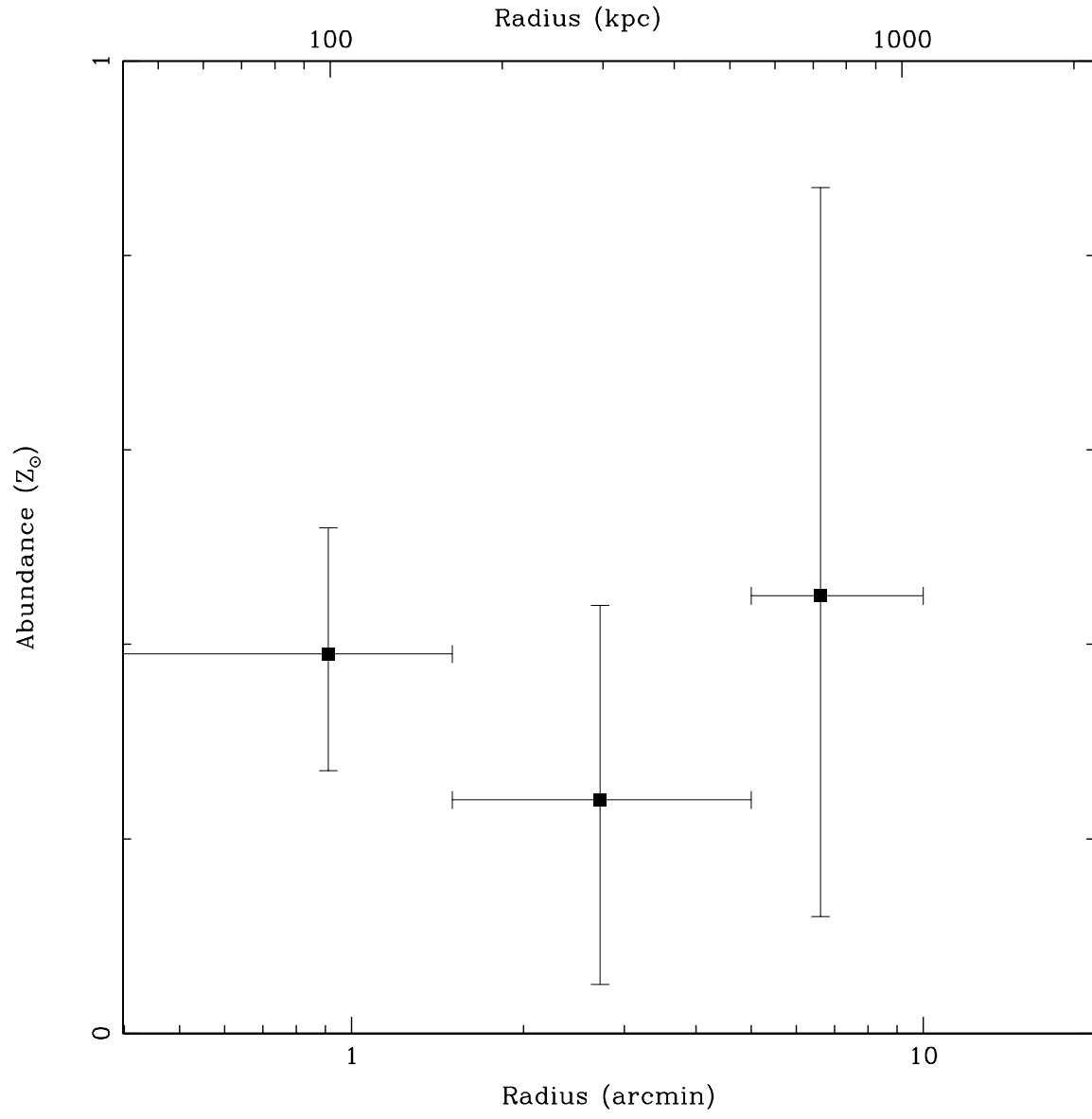


Figure 4

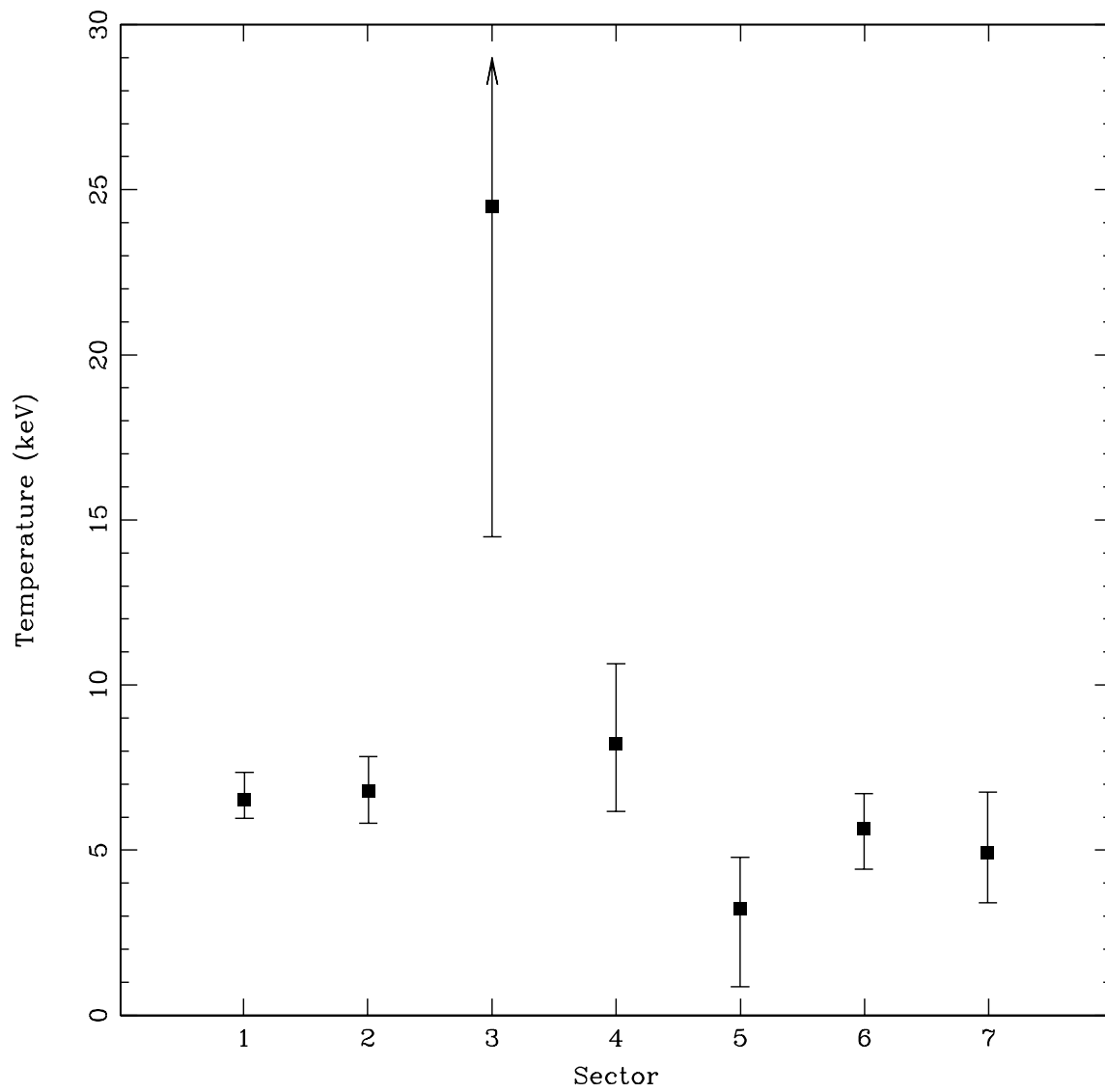


Figure 5

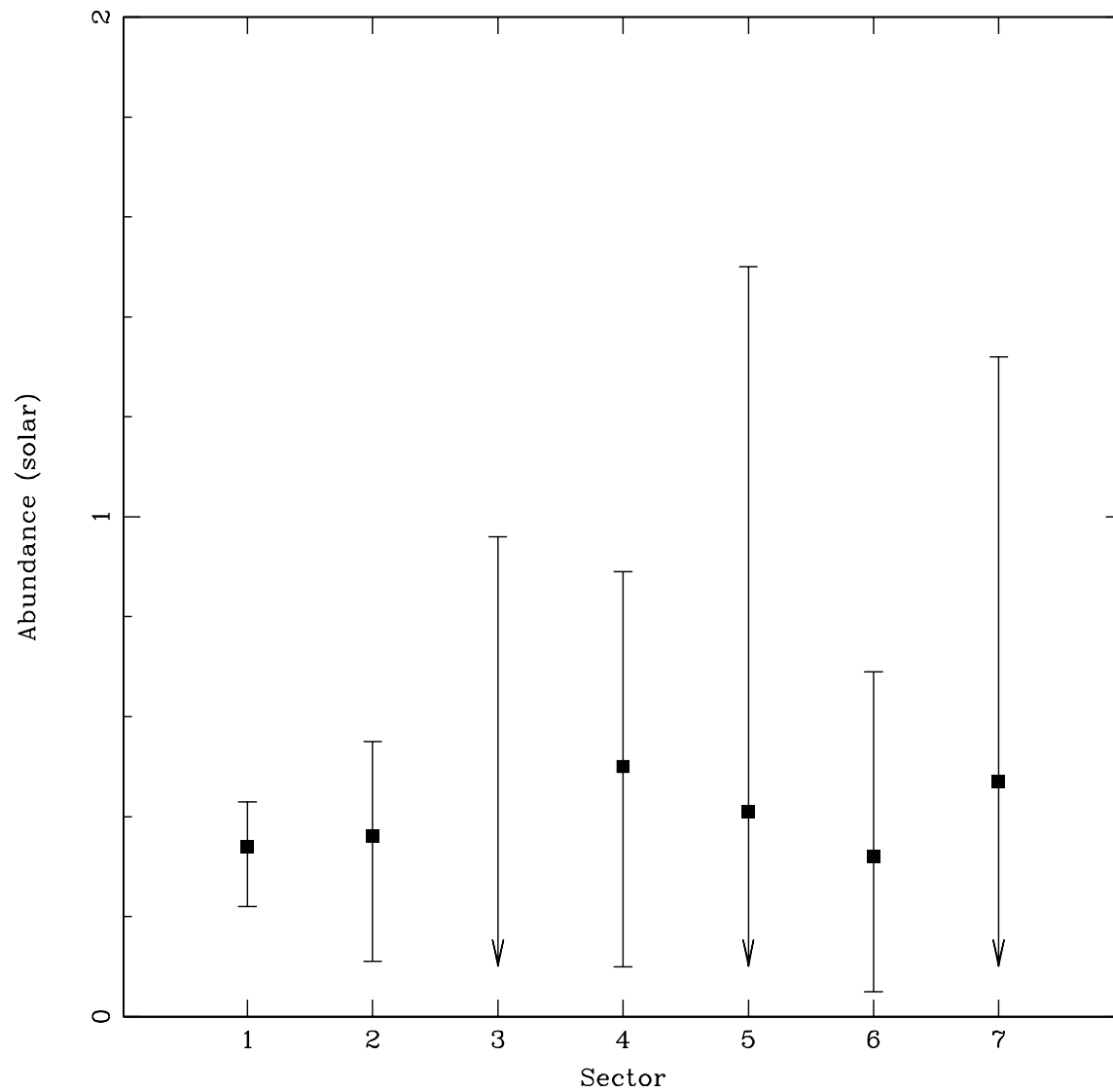


Figure 6

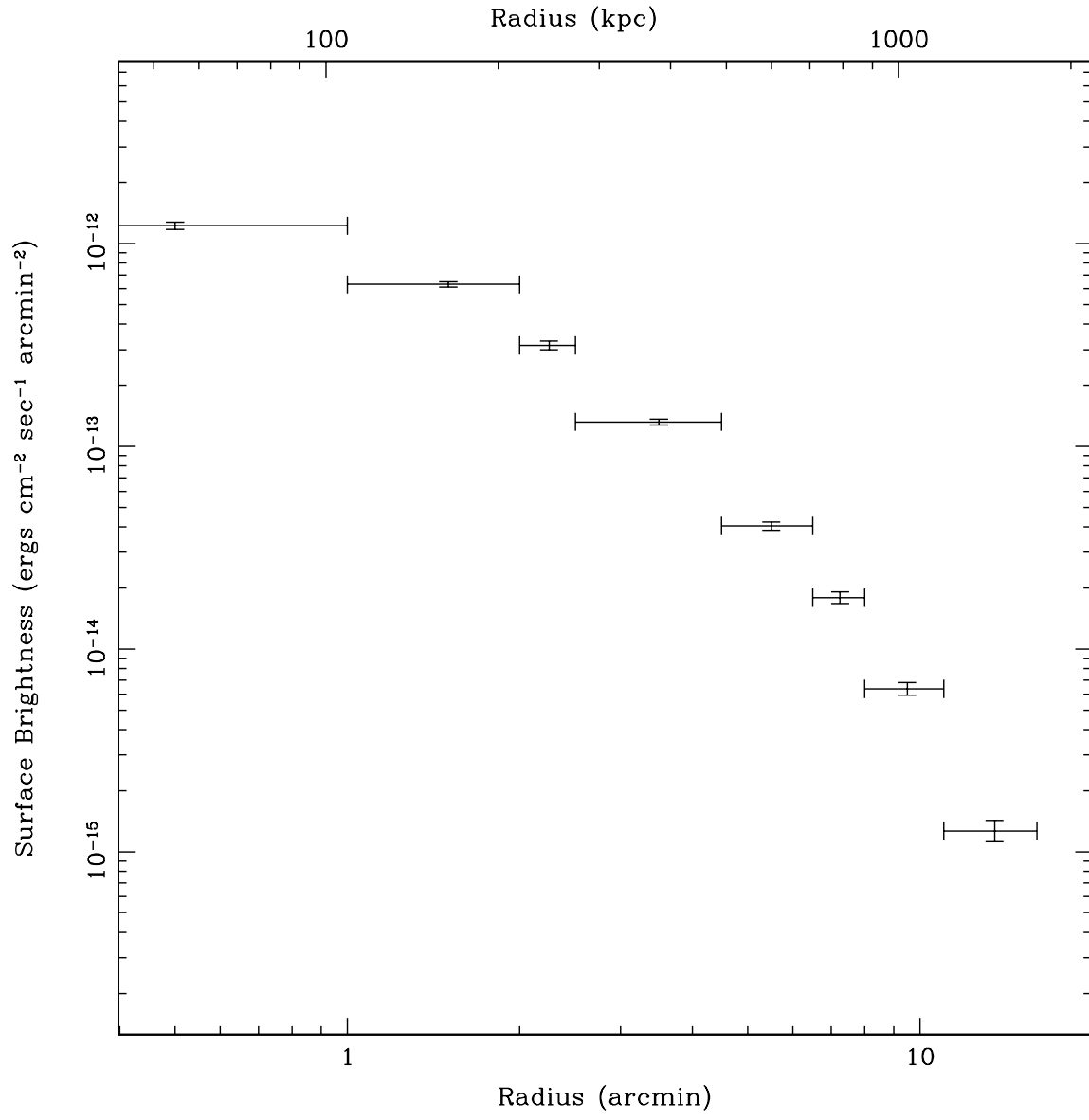


Figure 7

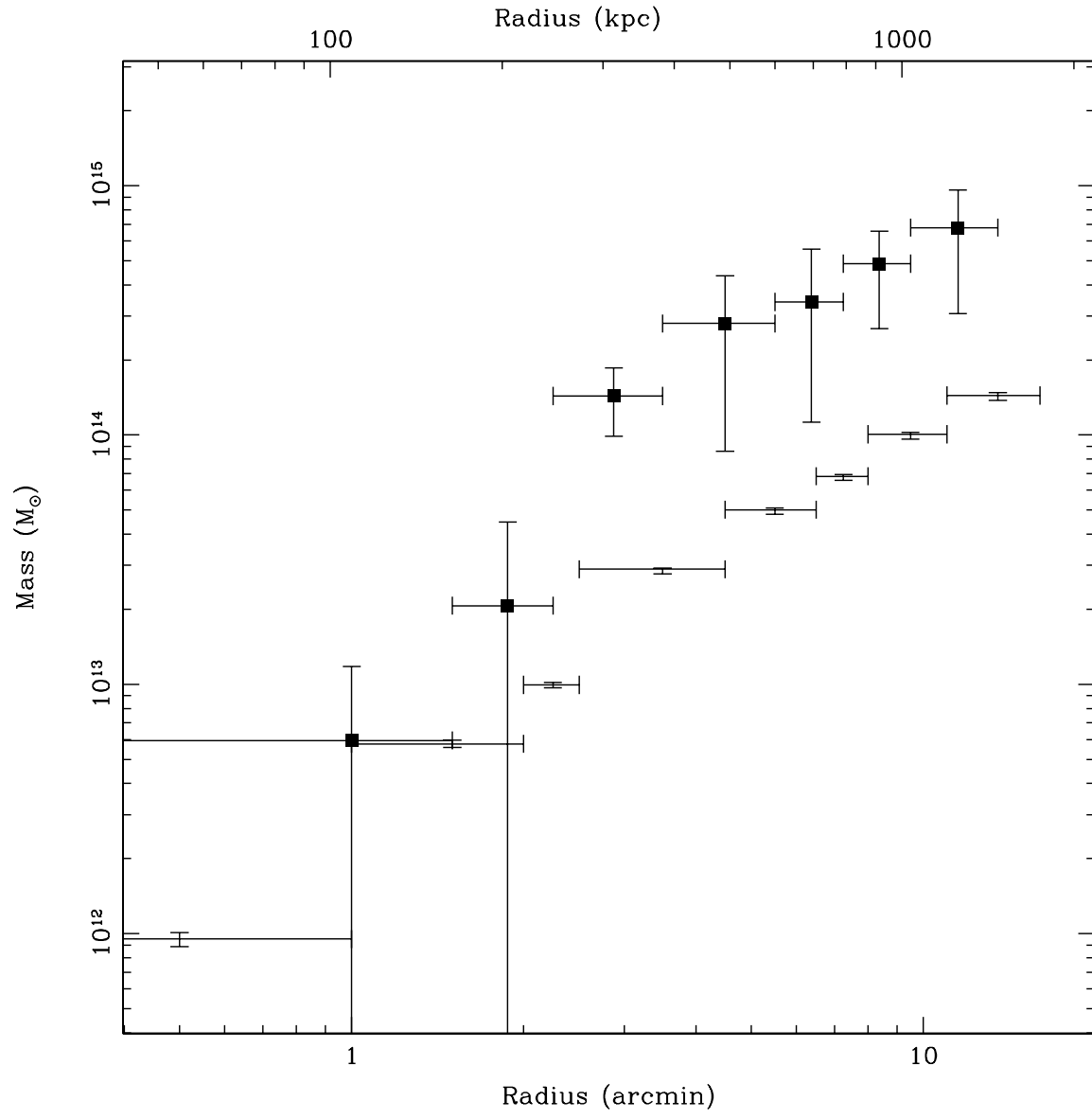


Figure 8

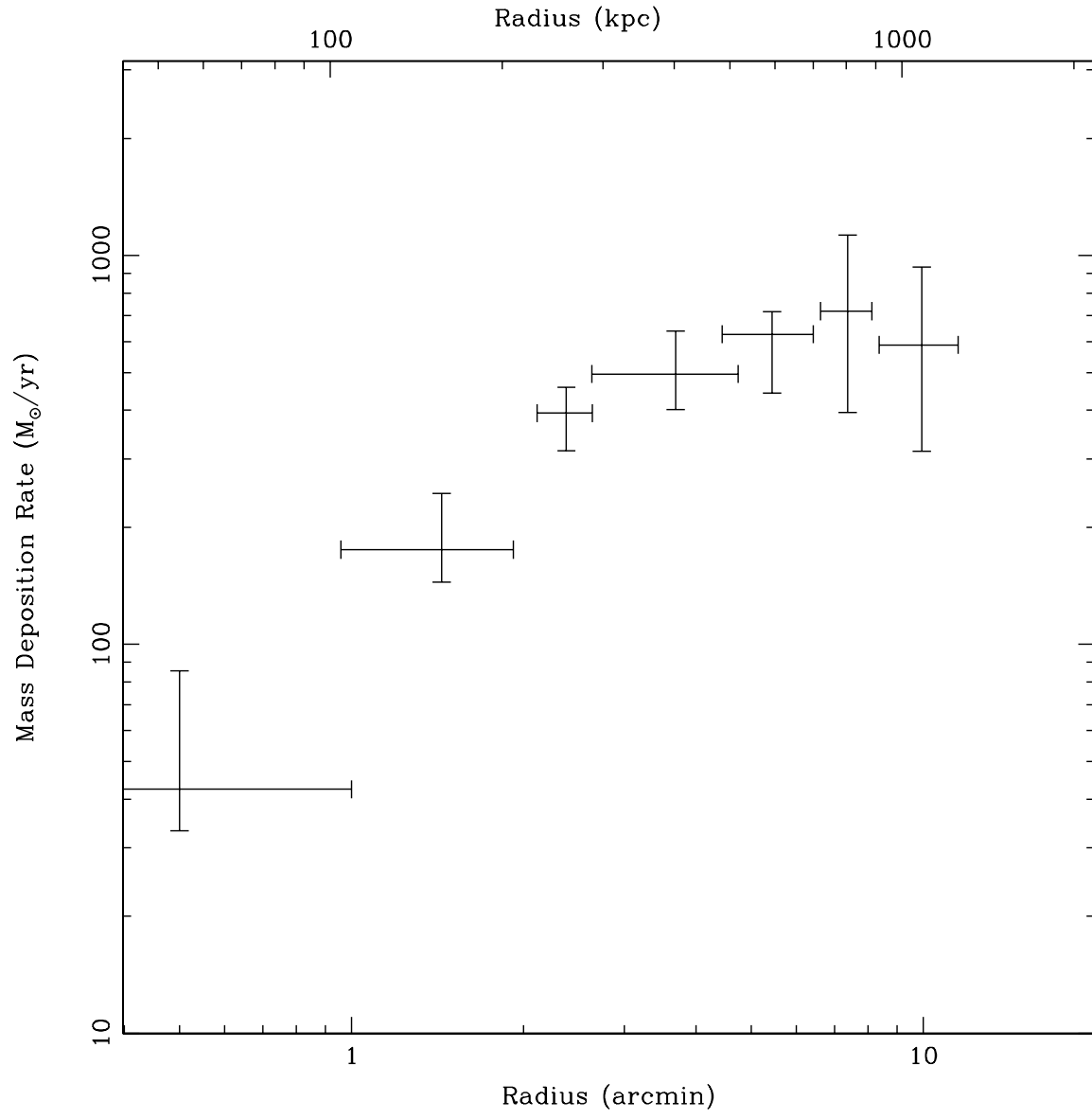


Figure 9

Table 1: Global Spectral Fits

	Single Temperature Model			Excess Absorption Model				Cooling Flow Model				
	kT (keV)	Z (Z_{\odot})	χ^2/ν	kT (keV)	Z (Z_{\odot})	ΔN_H (10^{20} cm^{-2})	χ^2/ν	kT (keV)	Z (Z_{\odot})	ΔN_H (10^{20} cm^{-2})	M ($M_{\odot} \text{ yr}^{-1}$)	χ^2/ν
<i>ASCA</i> GIS	$7.75^{+0.22}_{-0.21}$	0.30 ± 0.03	739.3/651 = 1.133	$7.59^{+0.30}_{-0.27}$	0.30 ± 0.03	1.03 (< 2.60)	737.7/650 = 1.132	$9.55^{+3.45}_{-0.99}$	0.34 ± 0.04	$9.82^{+1.97}_{-2.31}$	502^{+70}_{-193}	726.8/649 = 1.118
<i>ROSAT</i>	$5.44^{+1.17}_{-0.91}$	$1.23^{+1.35}_{-0.59}$	206.1/181 = 1.139	$3.11^{+1.24}_{-0.81}$	0.11 (< 0.50)	$3.70^{+2.54}_{-2.22}$	197.0/180 = 1.094	$4.71^{+20.90}_{-2.25}$	$0.37^{+1.33}_{-0.26}$	$2.73^{+2.69}_{-2.72}$	176 (< 499)	195.8/179 = 1.094
Combined	$7.69^{+0.22}_{-0.20}$	0.30 ± 0.03	966.2/834 = 1.159	$7.59^{+0.24}_{-0.22}$	0.30 ± 0.03	0.57 (< 1.26)	963.8/833 = 1.157	$8.64^{+0.67}_{-0.56}$	0.32 ± 0.04	$2.68^{+1.39}_{-1.21}$	214^{+100}_{-91}	946.9/832 = 1.138

All of the error bars or upper limits are at the 90% confidence level.

Table 2: ASCA Spectral Fits in Annuli

	Single Temperature Model			Excess Absorption Model				Cooling Flow Model				
	kT (keV)	Z (Z_{\odot})	χ^2/ν	kT (keV)	Z (Z_{\odot})	ΔN_H (10^{20} cm^{-2})	χ^2/ν	kT (keV)	Z (Z_{\odot})	ΔN_H (10^{20} cm^{-2})	\dot{M} ($M_{\odot} \text{ yr}^{-1}$)	χ^2/ν
0–1.5	$6.07^{+0.85}_{-0.57}$	$0.39^{+0.13}_{-0.12}$	53.1/96	$6.46^{+0.89}_{-0.80}$	$0.40^{+0.13}_{-0.14}$	1.32 (< 2.58)	50.8/95	$7.59^{+2.79}_{-1.64}$	$0.44^{+0.13}_{-0.16}$	< 1.50	156^{+100}_{-111}	50.7/94
1.5–5	$9.49^{+1.57}_{-1.43}$	$0.24^{+0.20}_{-0.19}$	= 0.553	$9.39^{+1.47}_{-1.33}$	$0.25^{+0.20}_{-0.21}$		= 0.535	$9.43^{+1.31}_{-1.38}$	$0.26^{+0.23}_{-0.21}$			= 0.539
5–10	$5.36^{+1.29}_{-1.26}$	$0.45^{+0.42}_{-0.33}$		$5.47^{+1.45}_{-1.14}$	$0.42^{+0.44}_{-0.29}$			$5.61^{+1.16}_{-1.33}$	$0.38^{+0.43}_{-0.28}$			

All of the error bars or upper limits are at the 90% confidence level.

Table 3: PSPC Annular Spectral Fits

Annulus (arcmin)	Single Temperature			Excess Absorption				Cooling Flow				
	kT (keV)	Z (Z_{\odot})	χ^2/ν	kT (keV)	Z (Z_{\odot})	ΔN_H (10^{20} cm^{-2})	χ^2/ν	kT (keV)	Z (Z_{\odot})	ΔN_H (10^{20} cm^{-2})	\dot{M} ($M_{\odot} \text{ yr}^{-1}$)	χ^2/ν
0–1.5	$3.40^{+0.99}_{-0.71}$	$0.52^{+0.48}_{-0.29}$	55.6/69 = 0.806	$1.98^{+0.74}_{-0.42}$	0.02 (< 0.22)	$4.59^{+3.25}_{-2.67}$	44.5/68 = 0.654	$3.47^{+19.86}_{-1.83}$	$0.19^{+0.40}_{-0.17}$	$3.16^{+3.13}_{-2.67}$	146 (< 380)	43.0/67 = 0.642
1.5–5	$7.89^{+1.62}_{-1.96}$	4.97 (> 1.25)	108.6/113 = 0.961	$3.58^{+2.24}_{-1.08}$	0.05 (< 0.86)	$3.99^{+2.83}_{-2.61}$	101.9/112 = 0.910	5.50 (> 2.59)	0.23 (< 1.06)	$3.27^{+1.82}_{-3.13}$	93 (< 392)	101.4/111 = 0.914
5–10	$8.73^{+25.28}_{-2.88}$... ^a	50.9/44 = 1.157	$5.89^{+10.57}_{-3.69}$... ^a	$3.72^{+7.63}_{-2.51}$	48.3/43 = 1.123					

^aAbundance value is not constrained

All of the error bars or upper limits are at the 90% confidence level.

Table 4:

ASCA Spectral Fits in Sectors			
Sector	Single Temperature		
	kT (keV)	Z (Z_{\odot})	χ^2/ν
1	$6.52^{+0.83}_{-0.55}$	$0.34^{+0.09}_{-0.12}$	145.08/216 = 0.672
2	$6.80^{+1.04}_{-0.99}$	$0.36^{+0.19}_{-0.25}$	
3	24.49 (> 15.48)	< 0.96	
4	$8.21^{+2.43}_{-2.04}$	$0.50^{+0.39}_{-0.40}$	
5	$3.23^{+1.55}_{-2.36}$	0.41 (< 1.50)	
6	$5.66^{+1.05}_{-1.24}$	$0.32^{+0.37}_{-0.27}$	
7	$4.92^{+1.84}_{-1.52}$	0.47 (< 1.32)	

All of the error bars or upper limits are at the 90% confidence level.